Int. J. Electrochem. Sci., 17 **(2022)** Article Number: 221179, doi: 10.20964/2022.11.83

International Journal of
ELECTROCHEMICAL
SCIENCE
www.electrochemsci.org

Synthesis of TiO_2@Fe_2O_3 Nanocomposites as effective Photocatalyst for degradation of p-nitophenol in oilfield wastewater

Xinxing He[1], Xiangjuan Meng[2], Jianyi Sun[2], Zebo Yuan[2], Yuyu He[2], Shijun Chen[3,]*

[1] Traim Oilfield Company, PetroChina, Korla, 841000, Xinjiang, China;
[2] Experimental and Testing Research Institute,
Traim Oilfield Company, PetroChina, Korla, 841000, Xinjiang, China;
[3].College of Chemistry and Chemical Engineering, Xi'an SHIYOU University, Xi'an, 710065, Shanxi Province,China.
[*]E-mail: csj19792018@sina.com

Received: 1 September 2022 / *Accepted:* 6 October 2022 / *Published:* 20 October 2022

The objective of this research was to create a TiO_2@Fe_2O_3 nanocomposite that would act as an effective photocatalyst for the degradation of p-nitrophenol (P-NP) as an organic compound in oilfield wastewater. Photocatalysts were synthesized using the ultrasonic-assisted impregnation technique. XRD and SEM analyses of photocatalyst structure and morphology revealed a combination of anatase-phase TiO_2 rod-like nanoparticles and hematite-phase spherical Fe_2O_3 nanoparticles in a TiO_2@Fe_2O_3 nanocomposite. Electrochemical studies revealed that the electron transfer rate of the TiO_2@Fe_2O_3 nanocomposite toward TiO_2 and Fe_2O_3 was increased. Optical studies revealed that the optical band gap values of TiO2, Fe2O3, and TiO_2@Fe_2O_3 nanocomposite were 2.10, 3.18, and 2.63 eV, respectively, demonstrating a significant enhancement to enable visible-light absorption of the heterostructured TiO_2@Fe_2O_3 nanocomposite. Photocatalytic degradation studies revealed that TiO_2, Fe_2O_3, and TiO_2@Fe_2O_3 nanocomposite had 100% removal efficiency after being exposed to 70, 100, and 60 minutes of solar light, respectively. The photocatalytic performance of TiO_2@Fe_2O_3 nanocomposite for P-NP treatment was compared to that of previously reported photocatalysts, and the results showed that TiO_2@Fe_2O_3 nanocomposite revealed a fast rate of photocatalytic treatment due to the synergistic effect of TiO_2 and Fe_2O_3 in nanocomposite. The results of the investigation into the performance of TiO_2@Fe_2O_3 nanocomposite for treatment of P-NP from oilfield wastewater revealed that TiO_2@Fe_2O_3 nanocomposite for treatment of P-NP from actual oilfield wastewater showed efficient photocatalytic degradation.

Keywords: Photocatalytic Treatment; TiO_2@Fe_2O_3 Nanocomposite; Ultrasonic-Assisted Impregnation Method; p-Nitrophenol; Organic Compounds; Oilfield Wastewater

1. INTRODUCTION

Oilfield wastewater is water that has been separated from the liquid produced by an oil well and contains varying mineral and organic contents such as fats, hydrocarbons, and petroleum fractions such as diesel oil, gasoline, kerosene, phenolic and nitrophenolic compounds, heavy metals, and cyanides that are associated with petroleum and natural gas or have been encountered during the search for oil and gas [1, 2]. Produced water refers to brackish and saline waters brought to the surface from underground formations [3, 4].

Many of these contaminants are toxic, and when they enter our water supplies, they can have serious short- and long-term health consequences [5-7]. As a result, oilfield wastewater must be extensively treated before it can be discharged [8, 9]. Chemical treatment methods include obsorption, Fenton oxidation, coagulation or flocculation combined with flotation and filtration, precipitation-flocculation, electroflotation, electrokinetic coagulation, photocatalysts, and biological treatment, which can remove multiple pollutants [10-14]. Photocatalysts of various types have been used to treat organic and inorganic polymeric compounds in wastewater [15, 16]. Photocatalysts are easier to operate and have lower capital and operational costs than methods such as flocculation, membrane filtration, and biological technologies [17, 18].

P-nitrophenol (P-NP; $C_6H_5NO_3$) also known as 4-nitrophenol or 4-hydroxynitrobenzene, is a phenolic compound with a nitro group opposite the hydroxyl group on the benzene ring. P-NP is used in the pharmaceutical, fungicide, insecticide, dye, and leather industries. P-NP can be used to measure pH [19, 20]. It is a byproduct of the synthesis of paracetamol [21, 22]. Due to chemical oxygen demand and total organic carbon, oilfield wastewaters contain phenol and nitrophenol. P-NP causes irritation of the eyes, skin, and respiratory tract [23, 24]. It could also cause inflammation in those areas. It interacts with the blood late and produces methaemoglobin, which causes methemoglobinemia and can result in cyanosis, confusion, and unconsciousness [25-27]. It causes abdominal pain and vomiting when consumed. Prolonged skin contact may result in an allergic reaction, headaches, drowsiness, and cyanosis. Despite the fact that many researchers have investigated the use of nanocomposites and metal oxides for the photocatalytic degradation of dyes, no research has been conducted on the photocatalytic and electrochemical performance of metal oxide nanocomposites for the degradation of organic compounds in oilfield wastewater. As a result, the goal of this study was to create a $TiO_2@Fe_2O_3$ nanocomposite that would act as an effective photocatalyst for the degradation of P-NP as an organic compound in oilfield wastewater.

2. MATERIALS AND METHOD

2.1. Preparation of photocatalyst

The ultrasonic-assisted impregnation technique was used for synthesizing photocatalysts [28]. For preparation $TiO_2@Fe_2O_3$ nanocomposite, 2 g of TiO_2 nano powder (<100 nm particle size, 99.5%, Sigma-Aldrich) was mixed with 60 mL of 0.6 M $Fe(NO_3)_3.9H_2O$ (99.95%, Sigma-Aldrich) and 15 mL

of ethanol (≥ 99.9 %, Merck Millipore, Germany). Next, the mixture was stirred for 2 hours at room temperature, and it was sonicated for 1 hour. Subsequently, the mixture was transferred in oven at 55 °C for 30 minutes to completely evaporate the ethanol. Then, the mixture was calcined at 285 °C for 7 hours. For synthesizing pure Fe_2O_3, the same process was performed without TiO_2 nanopowder. For synthesizing Fe_2O_3, the same process was performed without TiO_2 nanopowder.

2.2. Characterization and instruments

The crystallographic studies of the photocatalysts were performed using a Shimadzu X-ray diffractometer (XRD)-6000 using Cu Kα radiation. The morphology of synthesized photocatalysts was characterized by scanning electron microscopy (Super Scan SS-550, Shimadzu, Kyoto, Japan). UV/Vis absorption information was obtained on a Shimadzu UV-2550 UV/Vis spectrometer in the range of 200–800 nm. Electrochemical studies were conducted on cyclic voltammetry (CV) using an electrochemical workstation potentiostat galvanostat (CS350, Wuhan Corrtest Instruments Corp., Ltd., China) in the three-electrode configuration containing a photocatalyst-modified ITO-coated glass as a working electrode, platinum foil as a counter electrode and Ag/AgCl as a reference electrode. Electrochemical studies were carried out in a 1 mM $Fe(CN)_6^{3-/4-}$ (98%, Merck millipore, Germany) electrolyte at a potential range of -0.4 V to 0.8V at a scan rate of 100 mV/s.

2.3. Photocatalytic measurements.

The photocatalytic degradation measurements were carried out in batch photoreactor contained a cylindrical flask made of Pyrex under solar light illumination with a 300 W xenon lamp (Jiangmen Uvir Lighting Factory., China) which located in the center of the reactor and the distance between the lamp and solution in reactor was 8 cm. During photocatalytic experiments, the photoreactor was wrapped in aluminum foil to avoid any illumination by ambient light. For the treatment of P-NP, 1 mg of synthesized photocatalysts were added into 300 mL of different concentrations of P-NP (10, 20, 50, 100 and 200 mg/L) solutions under magnetic stirring. Before the photocatalytic degradation measurements, the mixture of dye and photocatalyst was magnetically stirred in the dark condition for 30 minutes to reach the desorbance-absorbance equilibrium between the P-NP molecules and photocatalyst particles in the dark. Subsequently, the mixture was exposed to solar illumination for different times to accomplish the photocatalytic reactions under magnetic stirring. The obtained P-NP samples from the photocatalytic reactions were collected and centrifuged at 1000 rpm for 5 minutes to remove photocatalyst particles. Then, the degraded P-NP samples were analyzed by UV-vis spectroscopy (Shimadzu UV-2550 UV/Vis, Kyoto, Japan) as the absorbance at 317 nm [29, 30]. The removal efficiency can be determined by the following equation [31, 32]:

$$\text{Removal efficiency (\%)} = \frac{C_0 - C_t}{C_0} \times 100 \qquad (1)$$

Where C_0 refers the initial concentration of P-NP and C_t is the concentration of P-NP after accomplish the photocatalytic reactions at time t (min).

3. RESULTS AND DISCUSSION

3.1. Analyses of Structure and morphology of photocatalysts

Figure 1 shows XRD patterns of TiO_2, Fe_2O_3, and $TiO_2@Fe_2O_3$ nanocomposite powders. TiO2 diffractogram shows clear peaks at 25.32°, 37.80°, 47.88°, 54.50°, 62.87°, 69.71°, and 75.13°, corresponding to (101), (004), (200), (211), (204), (220), and (301) reflection planes, respectively, which are related to TiO_2 anatase structure [33-35]. The peaks in the Fe_2O_3 diffractogram at 24.03°, 32.98°, 35.40°, 40.73°, 49.29°, 54.01°, 57.32°, 62.35°, and 63.97° that are indexed to (012), (104), (110), (113), (024), (116), (018), (214), and (030) diffraction planes, respectively, indicate the successful formation of the hematit structure of Fe_2O_3 (α-Fe_2O_3) [36-38]. XRD patterns of $TiO_2@Fe_2O_3$ nanocomposite show all the reflection peaks that are assigned to the anatase phase of TiO_2 and hematite phase of Fe_2O_3, and demonetarize that there are no secondary phases, indicating the combination of TiO_2 and Fe_2O_3 nanoparticles in $TiO_2@Fe_2O_3$ nanocomposite.

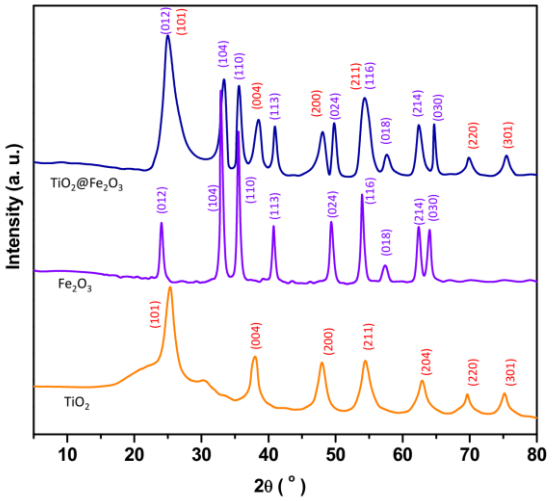

Figure 1. XRD patterns of powders of TiO_2, Fe_2O_3 and $TiO_2@Fe_2O_3$ nanocomposite.

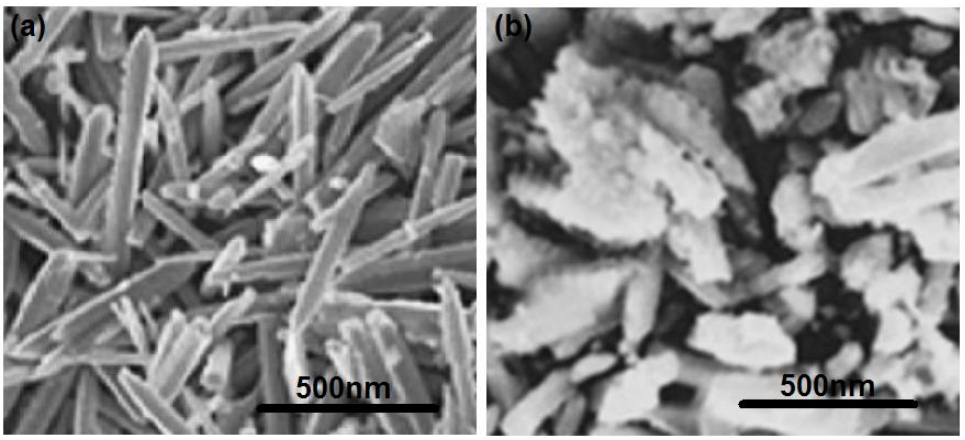

Figure 2. SEM image of (a) TiO_2 and (b) $TiO_2@Fe_2O_3$ nanocomposites

Figure 2 shows SEM images of the morphology of TiO_2 and $TiO_2@Fe_2O_3$ nanocomposites. Figure 2a shows that TiO_2 nanoparticles are successfully agglomerated with a well-uniform rod-like with an average width of 100 nm and an average length of 1µm. SEM images of $TiO_2@Fe_2O_3$ nanocomposites show spherical Fe_2O_3 nanoparticles attached to the surface of TiO_2 rod-like shape nanoparticles, forming a hetero-interface between the Fe_2O_3 and TiO_2 nanoparticles (Fig. 2b). As can be seen, the $TiO_2@Fe_2O_3$ nanocomposite has a higher effective surface area because the presence of both Fe_2O_3 and TiO_2 nanoparticles prevents nanoparticle agglomeration [39, 40].

3.2. Electrochemical studies

CV was used to investigate the electrochemical properties of TiO_2, Fe_2O_3 and $TiO_2@Fe_2O_3$ nanocomposite modified ITO electrodes in 1 mM $Fe(CN)_6^{3-/4-}$ electrolyte at a potential range of -0.4 V to 0.8 V at a scan rate of 100 mV/s. Figure 3 exhibits the CV curves of modified electrodes with a pair of redox peaks and peak-to-peak separation (ΔEp) of 0.33, 0.45 and 0.22 V for TiO_2, Fe_2O_3 and $TiO_2@Fe_2O_3$ nanocomposites on a modified ITO electrode, respectively. As seen, the highest peak currents and lowest peak-to-peak separation potential are observed for the $TiO_2@Fe_2O_3$ nanocomposite modified ITO electrode, implying that the modification of the electrode surface with the TiO_2 and Fe_2O_3 nanostructures increases the peak currents and decrease the peak-to-peak separation potential which indicates an enhancement of the electron transfer rate [41-43]. These results are the outcome of smaller particle size, a large electroactive surface area and numerous electroactive sites of the $TiO_2@Fe_2O_3$ nanocomposite modified electrode that are in agreement with the SEM results.

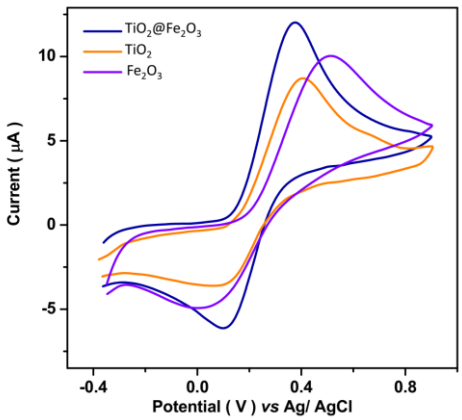

Figure 3. CV curves of TiO_2, Fe_2O_3 and $TiO_2@Fe_2O_3$ nanocomposite modified ITO electrode in 1 mM $Fe(CN)_6^{3-/4-}$ electrolyte at potential range -0.4 V to 0.8V at scan rate of 100 mV/s.

3.3. Optical studies

The optical absorbance spectra of TiO_2, Fe_2O_3 and $TiO_2@Fe_2O_3$ nanocomposite are depicted in Figure 4a. As observed, the UV-Vis absorption edges of a pure TiO_2 NPs sample are approximately ~

329 nm, which is a result of the electron transition from O2p to Ti3d states [44, 45]. UV-Vis absorbance spectra of Fe_2O_3 NPs show an absorption edge at ~ 560 nm, indicating a strong absorption peak in the visible light range [46], and TiO_2@Fe_2O_3 nanocomposite exhibits a greater light absorption threshold in the UV range with absorption edges at ~ 380 nm. The absorption coefficient (α) and photon energy (hν) can be related by [47, 48].

$$(\alpha h\nu)^2 = A(h\nu - Eg) \qquad (2)$$

In this equation, A is a constant, and Eg is the optical band gap. The Eg values of samples can be determined from a Tauc plot of $(\alpha h\nu)^2$ versus the photon energy axis in Figure 4b. As found, the Eg values of TiO_2, Fe_2O_3 and TiO_2@Fe_2O_3 nanocomposite are determined to be 2.10, 3.18 and 2.63 eV, respectively. As seen, the observed red shift in the absorption edge in TiO_2@Fe_2O_3 nanocomposite toward the pure TiO_2 NPs sample results to decrease in the band gap value of nanocomposite, and boosted visible-light absorption can be related to a sub-band-gap transition between 3d electrons of Fe^{3+} and TiO_2 conduction or valence band [49-51], demonstrated a significant enhancement to enable the visible-light absorption of the heterostructured TiO_2@Fe_2O_3 nanocomposite. Hence, Fe^{3+} shows the capability to create the novel narrowing energy levels in the band gap of TiO_2 and decrease the band gap with active photo-excitation between the valence band and conduction band [52, 53]. It is expected to have a remarkable visible light absorption, coupled with the active hematite and anatase phases and synergistic effect and heterojunction formed between TiO_2 and Fe_2O_3 [54-56]. Additionally, it can be attributed to the increased surface area of nanocomposites, according to SEM results because of the combination and interaction between TiO_2 NPs and Fe_2O_3 NPs. The high specific surface area of nanocomposites provides a larger interfacial contact region between two components, which improves the separation and migration of photo-generated charges facilitates the photo-generated charge transfer across the interface [57-59].

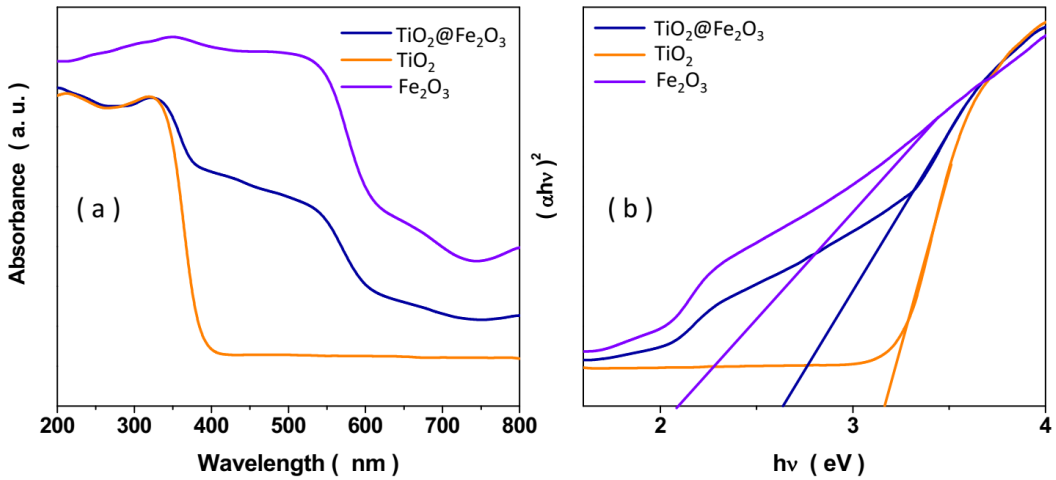

Figure 4. (a) Optical absorbance spectra of TiO_2, Fe_2O_3 and TiO_2@Fe_2O_3 nanocomposite and (b) Tauc plot in $(\alpha h\nu)^2$ versus photon energy.

3.4. Photocatalytic degradation studies

The removal efficiency of 300 ml of 50 mg/L P-NP solution in the absence (blank sample) and presence of photocatalysts are displayed in Figure 5. For a blank sample, the removal efficiency

reaches 4% after exposing it to the solar light for 2 hours. The removal efficiency in the presence of TiO_2, Fe_2O_3 and $TiO_2@Fe_2O_3$ nanocomposite is reached at 32.8%, 26.0% and 62.1% after 20 minutes of solar illumination, and 100% treatment of P-NP is obtained for TiO_2, Fe_2O_3 and $TiO_2@Fe_2O_3$ nanocomposite after exposure to 70, 100 and 60 minutes of solar light, respectively. Hence, these findings illustrate the fast photocatalytic treatment rate of P-NP in presence of $TiO_2@Fe_2O_3$ nanocomposite toward other photocatalysts which confirms structural, electrochemical and optical results that correspond to a larger effective surface area, the formation of more numerous of electro-active sites, efficient photo-generated electron and hole separation in the created heterojunction between TiO_2 and Fe_2O_3 in $TiO_2@Fe_2O_3$ nanocomposite, which can meanwhile effectively extend the spreading distance and the separation time. This enhancement is predominantly associated with to ameliorate the separation of photo-generated electron–hole pairs and improvement of migration efficiency due to formation heterojunction [60, 61]. The conduction band of Fe_2O_3 is lower than that of TiO2, while the valence band of Fe_2O_3 is higher than that of TiO_2, thereby forming a heterostructured $TiO_2@Fe_2O_3$ nanocomposite with conventional type-I heterojunctions [62, 63]. During light illumination, the photo-generated electrons and holes of TiO_2 can be quickly transferred to the conduction band and valence band of Fe_2O_3, indicating an effective decrease in the recombination rate of photo-generated electron-hole pairs of TiO_2. Subsequently, the photo-generated electrons in the conduction band of Fe_2O_3 can react with O_2 to create the superoxide radical (O_2^-), while the photo-generated holes in the valence band of Fe_2O_3 can react with H_2O and OH^- to generate the hydroxyl radicals ($^{\bullet}OH$). Afterwards, the generated O_2^- and $^{\bullet}OH$ can act as oxidants for the degradation the P-NP on the photocatalyst surface [64]. Furthermore, Fe_2O_3 with a narrower band gap can be easily excited to form electron-hole pairs in photocatalytic reactions.

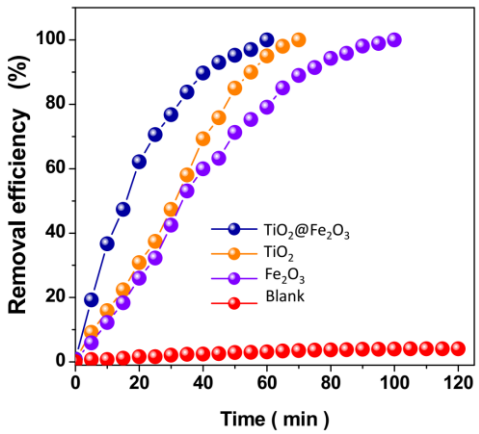

Figure 5. The removal efficiency of 300 ml of 50 mg/L P-NP solution in blank sample and presence of g TiO_2, Fe_2O_3 and $TiO_2@Fe_2O_3$ nanocomposite photocatalysts under solar light illumination.

The removal efficiency of $TiO_2@Fe_2O_3$ nanocomposite for treatment of different concentrations of P-NP under solar light illumination is shown in Figure 6. The complete treatment of 10, 20, 50, 100 and 200 mg/L of P-NP is obtained after 35, 45, 60, 75 and 120 minutes of solar light illumination, respectively. Findings reveal that removal efficiency decreases as the initial P-NP concentration increases. Table 2 compares the photocatalytic performance of $TiO_2@Fe_2O_3$

nanocomposite for P-NP treatment with previously reported photocatalysts. It is observed that TiO_2@Fe_2O_3 nanocomposite reveals a fast rate of photocatalytic treatment because of synergistic effect of TiO_2 and Fe_2O_3 in nanocomposite to form a great effective surface area and heterojunction to enhance the efficiency of photo-generated electrons, hole population, and photocatalytic reactions.

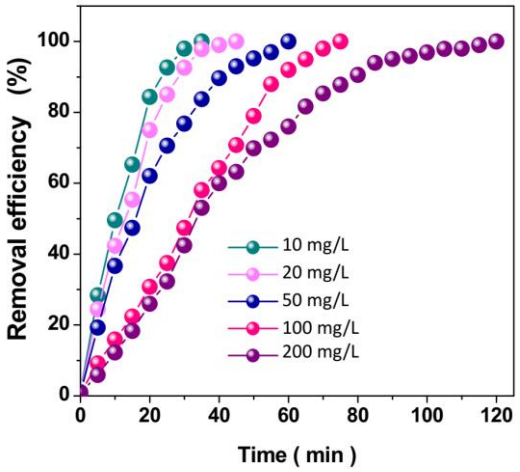

Figure 6. The removal efficiency of TiO_2@Fe_2O_3 nanocomposite for treatment different concentrations of P-NP under solar light illumination.

Table 2. The photocatalytic performance of TiO_2@Fe_2O_3 nanocomposite for treatment P-NP and other reported photocatalyst in the literatures.

Photocatalyst	**Amount of** P-NP **(mg/L)**	**Light source**	**Removal efficiency (%)**	**Degradation time (minute)**	**Ref.**
TiO_2/H_2O_2	10	UV	94.6	240	[65]
Carbon nitride	10	UV	100	80	[66]
ZnO	15	Solar	100	90	[67]
SnO_2/GO	20	UV	95.6	90	[68]
BiOCl/$Ti_3C_2T_x$	20	Simulated sunlight	97.86	50	[69]
Si–α-Fe_2O_3	20.86	UV	66	120	[70]
TiO_2@Fe_2O_3	10	Solar	100	35	Present study
	20			45	
	50			60	
	100			75	
	200			120	

3.5. P-NP treatment from oilfield wastewater

The performance of TiO_2, Fe_2O_3 and TiO_2@Fe_2O_3 nanocomposites photocatalysts for treatment of P-NP from oilfield wastewater was examined. Figure 7 demonestrates the removal efficiency of photocatalysts for treatment of the 300 mL of 50 mg/L P-NP solution prepared from actual oilfield

wastewater (Daqing oilfield, Heilongjiang, China). As shown, the total removal efficiency of the real sample is achieved after 85, 110 and 68 minutes of solar light illumination in presence of TiO_2, Fe_2O_3 and $TiO_2@Fe_2O_3$ nanocomposites, respectively. Thus, these results show the efficient photocatalytic degradation of $TiO_2@Fe_2O_3$ nanocomposite for the treatment of P-NP from actual oilfield wastewater.

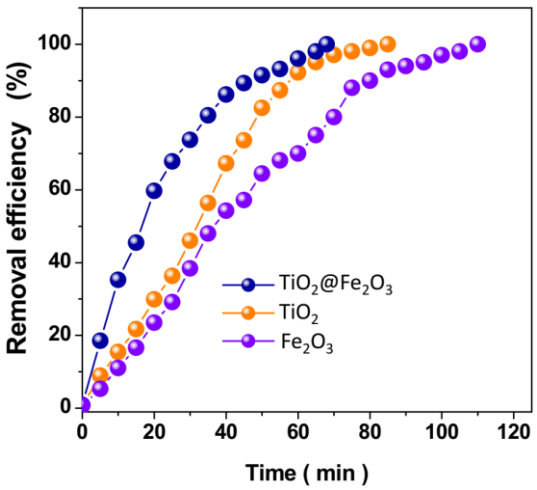

Figure 7. The removal efficiency of TiO_2, Fe_2O_3 and $TiO_2@Fe_2O_3$ nanocomposites for treatment the 300 mL of 50 mg/L P-NP solution prepared from actual oilfield wastewater.

4. CONCLUSION

This work was done to create a $TiO_2@Fe_2O_3$ nanocomposite that can be used as an effective photocatalyst for the degradation of P-NP as other organic compounds in oilfield wastewater. Photocatalysts were synthesized using the ultrasonic-assisted impregnation technique. Structure and morphology analyses of photocatalysts revealed that TiO_2 rod-like nanoparticles and spherical Fe_2O_3 nanoparticles should be combined to form a $TiO_2@Fe_2O_3$ nanocomposite. Electrochemical studies revealed that the electron transfer rate of the $TiO_2@Fe_2O_3$ nanocomposite toward TiO_2 and Fe2O3 was increased. Optical studies revealed that the optical band gap values of TiO_2, Fe_2O_3, and $TiO_2@Fe_2O_3$ nanocomposite were 2.10, 3.18, and 2.63 eV, respectively, demonstrating a significant enhancement to enable visible-light absorption of the heterostructured $TiO_2@Fe_2O_3$ nanocomposite. Photocatalytic degradation studies revealed that TiO_2, Fe_2O_3, and $TiO_2@Fe_2O_3$ nanocomposite had 100% removal efficiency after being exposed to 70, 100, and 60 minutes of solar light, respectively. The increase in the rate of P-NP treatment in $TiO_2@Fe_2O_3$ nanocomposite was primarily associated with improved separation of photo-generated electron-hole pairs and increased migration efficiency due to heterojunction. The photocatalytic degradation of $TiO_2@Fe_2O_3$ nanocomposite for treatment of P-NP from actual oilfield wastewater was investigated, and the results demonstrated the efficient photocatalytic degradation of $TiO_2@Fe_2O_3$ nanocomposite for treatment of P-NP from actual oilfield wastewater.

References

1. H.N. Nassar, W.I. El-Azab and N.S. El-Gendy, *Journal of Hazardous Materials*, 422 (2022)

126845.
2. D. Quick, *Money*, 23 (2010) 50.
3. A. Echchelh, T. Hess and R. Sakrabani, *Agricultural Water Management*, 206 (2018) 124.
4. X. Mo, X. Liu, J. Chen, S. Zhu, W. Xu, K. Tan, Q. Wang, Z. Lin and W. Liu, *Environmental Science: Nano*, 9 (2022) 1617.
5. S. Adithya, R.S. Jayaraman, A. Krishnan, R. Malolan, K.P. Gopinath, J. Arun, W. Kim and M. Govarthanan, *Chemosphere*, 271 (2021) 129866.
6. X. Sun, J. Li, X. Sun, J. Zheng, Z. Wu, W. Liu, D. Zhao and Z. Lin, *Chemical Engineering Journal*, 421 (2021) 129683.
7. M. Yang, C. Li, Y. Zhang, D. Jia, X. Zhang, Y. Hou, R. Li and J. Wang, *International Journal of Machine Tools and Manufacture*, 122 (2017) 55.
8. H. Maleh, M. Alizadeh, F. Karimi, M. Baghayeri, L. Fu, J. Rouhi, C. Karaman, O. Karaman and R. Boukherroub, *Chemosphere*, (2021) 132928.
9. N. Naderi, M. Hashim and J. Rouhi, *International Journal of Electrochemical Science*, 7 (2012) 8481.
10. P. Kumar, R. Agnihotri, K.L. Wasewar, H. Uslu and C. Yoo, *Desalination and Water Treatment*, 50 (2012) 226.
11. V. Nogueira, I. Lopes, A. Freitas, T. Rocha-Santos, F. Gonçalves, A. Duarte and R. Pereira, *Ecotoxicology and environmental safety*, 115 (2015) 234.
12. L. Yu and B. Tang, *International Journal of Electrochemical Science*, 16 (2021) 210915.
13. F. Ban, H. Nan, Q. Jin and Y. Wang, *International Journal of Electrochemical Science*, 16 (2021) 210648.
14. J. Rouhi, C.R. Ooi, S. Mahmud and M.R. Mahmood, *Materials Letters*, 147 (2015) 34.
15. B. Pal, M. Sharon and G. Nogami, *Materials Chemistry and Physics*, 59 (1999) 254.
16. M. Yang, C. Li, Y. Zhang, D. Jia, R. Li, Y. Hou, H. Cao and J. Wang, *Ceramics International*, 45 (2019) 14908.
17. F. Liu, S. Dong, Z. Zhang, X. Dai, Y. Xin, X. Wang, K. Liu, Z. Yuan, J. Zhang and M. Chen, *International Journal of Electrochemical Science*, 14 (2019) 9122.
18. C. Shi, Z. Wu, F. Yang and Y. Tang, *Solid State Sciences*, 119 (2021) 106702.
19. F. Chen, J. Ma, Y. Zhu, X. Li, H. Yu and Y. Sun, *Journal of Hazardous Materials*, 426 (2022) 128064.
20. J. Rouhi, M. Alimanesh, R. Dalvand, C.R. Ooi, S. Mahmud and M.R. Mahmood, *Ceramics International*, 40 (2014) 11193.
21. P.T. Thi, T. Van Khai, T.X. Diem, C.N.T. Nghia, T.T.T. Ngan, N.N. Vinh and N.M. Hien, *Materials Research Express*, 8 (2021) 105009.
22. H. Liu, J. Yang, Y. Jia, Z. Wang, M. Jiang, K. Shen, H. Zhao, Y. Guo, Y. Guo and L. Wang, *Environmental Science & Technology*, 55 (2021) 10734.
23. Z. Huang, S. Cao, J. Yu, X. Tang, Y. Guo, Y. Guo, L. Wang, S. Dai and W. Zhan, *Environmental Science & Technology*, 56 (2022) 9661.
24. H. Karimi-Maleh, R. Darabi, M. Shabani-Nooshabadi, M. Baghayeri, F. Karimi, J. Rouhi, M. Alizadeh, O. Karaman, Y. Vasseghian and C. Karaman, *Food and Chemical Toxicology*, 162 (2022) 112907.
25. S.R. Saeed, M. Ajmal, I. Bibi, S.S. Shah and M. Siddiq, *Journal of Taibah University for Science*, 16 (2022) 472.
26. Z. Wu, C. Li, F. Zhang, S. Huang, F. Wang, X. Wang and H. Jiao, *Journal of Materials Chemistry C*, 10 (2022) 7443.
27. Y. Wang, C. Li, Y. Zhang, M. Yang, B. Li, L. Dong and J. Wang, *International Journal of Precision Engineering and Manufacturing-Green Technology*, 5 (2018) 327.
28. S.R. Mirmasoomi, M.M. Ghazi and M. Galedari, *Separation and Purification Technology*, 175 (2017) 418.

29. H. Xia, W. Zhang, Z. Yang, Z. Dai and Y. Yang, *Journal of Analytical Methods in Chemistry*, 2021 (2021) 6682722.
30. M.S. Samuel, S. Jose, E. Selvarajan, T. Mathimani and A. Pugazhendhi, *Journal of Photochemistry and Photobiology B: Biology*, 202 (2020) 111642.
31. T. Maggos, J. Bartzis, P. Leva and D. Kotzias, *Applied Physics A*, 89 (2007) 81.
32. M. Husairi, J. Rouhi, K. Alvin, Z. Atikah, M. Rusop and S. Abdullah, *Semiconductor Science and Technology*, 29 (2014) 075015.
33. X. Lü, P. Hao, G. Xie, J. Duan, L. Gao and B. Liu, *Sensors*, 19 (2019) 915.
34. Y. Wang, X. Wu, J. Liu, Z. Zhai, Z. Yang, J. Xia, S. Deng, X. Qu, H. Zhang and D. Wu, *Journal of Environmental Chemical Engineering*, 10 (2022) 107091.
35. J. Rouhi, S. Mahmud, S.D. Hutagalung and N. Naderi, *Electronics letters*, 48 (2012) 712.
36. M. Qayoom, K.A. Shah, A.H. Pandit, A. Firdous and G.N. Dar, *Journal of Electroceramics*, 45 (2020) 7.
37. K. Cai, X. Jing, Y. Zhang, L. Li and X. Lang, *International Journal of Energy Research*, 46 (2022) 14570.
38. H. Karimi-Maleh, C. Karaman, O. Karaman, F. Karimi, Y. Vasseghian, L. Fu, M. Baghayeri, J. Rouhi, P. Senthil Kumar and P.-L. Show, *Journal of Nanostructure in Chemistry*, (2022) 1.
39. J. Zhang, C. Li, Y. Zhang, M. Yang, D. Jia, G. Liu, Y. Hou, R. Li, N. Zhang and Q. Wu, *Journal of Cleaner Production*, 193 (2018) 236.
40. L. Tang, Y. Zhang, C. Li, Z. Zhou, X. Nie, Y. Chen, H. Cao, B. Liu, N. Zhang and Z. Said, *Chinese Journal of Mechanical Engineering*, 35 (2022) 1.
41. B.J. Venton and Q. Cao, *Analyst*, 145 (2020) 1158.
42. P. Liu, S. Li, L. Zhang, X. Yin and Y. Ma, *Catalysis Science & Technology*, 12 (2022) 4193.
43. M. Liu, C. Li, Y. Zhang, Q. An, M. Yang, T. Gao, C. Mao, B. Liu, H. Cao and X. Xu, *Frontiers of Mechanical Engineering*, 16 (2021) 649.
44. Z. Fan, F. Meng, J. Gong, H. Li, Z. Ding and B. Ding, *Journal of Materials Science: Materials in Electronics*, 27 (2016) 11866.
45. X. Wu, C. Li, Z. Zhou, X. Nie, Y. Chen, Y. Zhang, H. Cao, B. Liu, N. Zhang and Z. Said, *The International Journal of Advanced Manufacturing Technology*, 117 (2021) 2565.
46. C.-R. Zhang, L. Liu, J.-W. Zhe, N.-Z. Jin, L.-H. Yuan, Y.-H. Chen, Z.-Q. Wei, Y.-Z. Wu, Z.-J. Liu and H.-S. Chen, *Journal of molecular modeling*, 19 (2013) 1553.
47. A. Kumar, S. Billa, S. Chaudhary, A.K. Kumar, C.V. Ramana and D. Kim, *Inorganic Chemistry Communications*, 97 (2018) 191.
48. J. Rouhi, S. Mahmud, S.D. Hutagalung, N. Naderi, S. Kakooei and M.J. Abdullah, *Semiconductor Science and Technology*, 27 (2012) 065001.
49. M. Sołtys-Mróz, K. Syrek, J. Pierzchała, E. Wiercigroch, K. Malek and G.D. Sulka, *Applied Surface Science*, 517 (2020) 146195.
50. P. Dong, Y. Zhang, S. Zhu, Z. Nie, H. Ma, Q. Liu and J. Li, *Metals*, 12 (2022) 1160.
51. T. Gao, C. Li, Y. Wang, X. Liu, Q. An, H.N. Li, Y. Zhang, H. Cao, B. Liu and D. Wang, *Composite Structures*, 286 (2022) 115232.
52. S. George, S. Pokhrel, Z. Ji, B.L. Henderson, T. Xia, L. Li, J.I. Zink, A.E. Nel and L. Mädler, *Journal of the American Chemical Society*, 133 (2011) 11270.
53. X. Fan, G. Wei, X. Lin, X. Wang, Z. Si, X. Zhang, Q. Shao, S. Mangin, E. Fullerton and L. Jiang, *Matter*, 2 (2020) 1582.
54. K. Yao, P. Basnet, H. Sessions, G.K. Larsen, S.E.H. Murph and Y. Zhao, *Catalysis today*, 270 (2016) 51.
55. H.H. Mohamed, N.A. Alomair, S. Akhtar and T.E. Youssef, *Journal of Photochemistry and Photobiology A: Chemistry*, 382 (2019) 111951.
56. H. Li, Y. Zhang, C. Li, Z. Zhou, X. Nie, Y. Chen, H. Cao, B. Liu, N. Zhang and Z. Said, *The International Journal of Advanced Manufacturing Technology*, 120 (2022) 1.

57. Q. Sun, P. Hou, S. Wu, L. Yu and L. Dong, *Colloids and Surfaces A: Physicochemical and Engineering Aspects*, 628 (2021) 127304.
58. H. Karimi-Maleh, H. Beitollahi, P.S. Kumar, S. Tajik, P.M. Jahani, F. Karimi, C. Karaman, Y. Vasseghian, M. Baghayeri and J. Rouhi, *Food and Chemical Toxicology*, (2022) 112961.
59. D. Jia, Y. Zhang, C. Li, M. Yang, T. Gao, Z. Said and S. Sharma, *Tribology International*, 169 (2022) 107461.
60. J. Luo, X. Zhou, L. Ma and X. Xu, *Journal of Molecular Catalysis A: Chemical*, 410 (2015) 168.
61. H. Li, Y. Zhang, C. Li, Z. Zhou, X. Nie, Y. Chen, H. Cao, B. Liu, N. Zhang and Z. Said, *Korean Journal of Chemical Engineering*, 39 (2022) 1107.
62. R. Zhang, M. Sun, G. Zhao, G. Yin and B. Liu, *Applied Surface Science*, 475 (2019) 380.
63. B. Li, C. Li, Y. Zhang, Y. Wang, D. Jia and M. Yang, *Chinese Journal of Aeronautics*, 29 (2016) 1084.
64. B. Divband, A. Jodaei and M. Khatamian, *Iranian Journal of Catalysis*, 9 (2019) 63.
65. K.P. Mishra and P.R. Gogate, *Ultrasonics sonochemistry*, 18 (2011) 739.
66. J. Sun, J. Xu, A. Grafmueller, X. Huang, C. Liedel, G. Algara-Siller, M. Willinger, C. Yang, Y. Fu, X. Wang and M. Shalom, *Applied Catalysis B: Environmental*, 205 (2017) 1.
67. M. Sugiyama, Z. Salehi, M. Tokumura and Y. Kawase, *Water Science and Technology*, 65 (2012) 1882.
68. Y. Chen, F. Sun, Z. Huang, H. Chen, Z. Zhuang, Z. Pan, J. Long and F. Gu, *Applied Catalysis B: Environmental*, 215 (2017) 8.
69. C. Wang, J. Shen, R. Chen, F. Cao and B. Jin, *Applied Surface Science*, 519 (2020) 146175.
70. M. Tong, D. Sun, R. Zhang, H. Liu and R. Chen, *Journal of Alloys and Compounds*, 862 (2021) 158271.